



ELSEVIER

Contents lists available at ScienceDirect

Journal of Quantitative Spectroscopy & Radiative Transfer

journal homepage: www.elsevier.com/locate/jqsrt

Light transfer through semi-transparent glass panes supporting pendant droplets



Eylul Simsek^a, Keyong Zhu^b, Glareh N. Kashanchi^c, Megan J. Williams^a, Tiphaine Galy^a, Michal Marszewski^a, Sarah H. Tolbert^{c,d,e}, Laurent Pilon^{a,e,f,*}

^a Mechanical and Aerospace Engineering Department, University of California, Los Angeles, CA 90095-1597, USA

^b School of Aeronautical Science and Engineering, Beihang University, Beijing 100191, China

^c Department of Chemistry, University of California, Los Angeles, CA 90095-1569, USA

^d Department of Materials Science and Engineering, University of California, Los Angeles, CA 90095-1595, USA

^e California NanoSystems Institute, University of California, Los Angeles, CA 90095, USA

^f Institute of the Environment and Sustainability, University of California, Los Angeles, CA 90095, USA

ARTICLE INFO

Article history:

Received 5 September 2020

Revised 16 December 2020

Accepted 19 December 2020

Available online 24 December 2020

Keywords:

Dropwise condensation

Light scattering

Greenhouse cladding

Solar desalination

ABSTRACT

This paper quantifies experimentally the effect of pendant droplets condensed on the back of semi-transparent glass panes on their normal-hemispherical transmittance and reflectance in the visible and near-infrared. To enable sample characterization and ensure repeatability, acrylic droplets were deposited on the back side of 3 mm-thick soda-lime silicate glass slabs with or without hydrophobic surface treatment including perfluorinated silane, perfluorinated silane-coated silica nanoparticle monolayer, or Teflon coatings. The droplet contact angle θ_c was varied between 26° and 76° and the projected surface area coverage reached up to 60%. For contact angle θ_c smaller than the critical angle θ_{cr} for total internal reflection at the droplet/air interface, the presence of droplets did not significantly affect the normal-hemispherical transmittance and reflectance. However, for droplet contact angle $\theta_{cr} \leq \theta_c < 90^\circ$, the normal-hemispherical transmittance decreased significantly with increasing droplet contact angle and/or surface area coverage while the normal-hemispherical reflectance increased. The measurements of the normal-hemispherical transmittance were in excellent agreement with numerical predictions obtained from Monte Carlo Ray Tracing method. These results further validate our previous numerical simulations and the different optical regimes identified. The results of this study can provide guidelines for the design and operation of energy efficient flat-plate solar collectors, outdoor photobioreactors, greenhouses, solar desalination systems, and other solar energy conversion systems.

© 2020 Elsevier Ltd. All rights reserved.

1. Introduction

Pendant water droplets are often observed at the inner surface of semi-transparent plastic films or window covers of flat-plate solar collectors [1], outdoor photobioreactors [2,3], greenhouses [4–10], and solar desalination systems [11–13], as illustrated in Fig. 1. The water droplets can appear as a result of dropwise condensation where discrete droplets form and grow on the inner surface of the covers [14]. These water droplets have been shown to reduce light transmission through covers or windows due to absorption and/or back-scattering of light [15,16]. However, solar radiation is the energy source driving these different processes. Thus, the presence of droplets may negatively affect the perfor-

mance and overall energy efficiency of solar energy conversion systems [4–9,11–13,17,18].

Experiments reproducing condensation on the cladding of greenhouses and measuring the cover transmittance under different experimental conditions have been reported in the literature [4–9,17]. However, the water droplets in these experiments were difficult to characterize due to the dynamic nature of the condensation process and the outdoor conditions. Indeed, sufficiently large droplets roll off the surface and entrain others in their wake. Thus, the shape, size, location, and overall surface area coverage of the window by the water droplets change continuously during the course of the experiments and render droplet characterization and optical measurements extremely difficult. Alternatively, numerical simulations have predicted the normal-hemispherical transmittance and reflectance of windows supporting one non-absorbing cap-shaped droplet [19] or an ensemble of (i) ordered or randomly distributed, (ii) monodisperse or polydisperse, (iii) non-absorbing

* Corresponding author.

E-mail address: pilon@seas.ucla.edu (L. Pilon).

Nomenclature

d_p	droplet diameter (μm)
f_A	droplet surface area coverage (%)
H	glass thickness (mm)
I	radiation incident intensity ($\text{W}/\text{m}^2 \cdot \text{sr}$)
k	absorption index
L	glass length (mm)
m	complex index of refraction, $m = n + ik$
n	refractive index
R	reflectance (%)
T	transmittance (%)
W	glass width (mm)

Greek symbols

θ_c	droplet contact angle ($^\circ$)
θ_{cr}	critical angle for the droplet/air interface ($^\circ$)
θ_i	incident angle ($^\circ$)
κ	absorption coefficient ($1/\text{m}$)
λ	wavelength (nm)
ρ	interface reflectivity
σ	standard deviation in droplet size distribution

Subscription

a	refers to air
ag	refers to the air/glass interface
d	refers to droplet
g	refers to glass
nh	refers to normal-hemispherical
nn	refers to normal-normal
w	refers to glass pane of window
λ	refers to spectral variables

or absorbing cap-shaped droplets [20,21]. Unfortunately, to the best of our knowledge, experimental validation of these complex numerical simulations has not been reported in the literature.

The present study aims to assess experimentally the effects of pendant droplets on light transfer through semi-transparent glass panes. Particular attention was paid to the effects of droplet contact angle and surface area coverage. To do so, glass slabs supporting droplets with different contact angles and projected surface area coverages were prepared. The normal-hemispherical transmittance and reflectance of each sample was measured in the visible and near-infrared part of the electromagnetic spectrum. The results can provide guidelines for the design and operation of energy efficient flat-plate solar collectors, photobioreactors, greenhouses, solar stills, and other solar energy conversion systems.

2. Background

2.1. Modeling

Tow [19] used the Monte Carlo Ray Tracing (MCRT) method to numerically investigate light transfer through a 3 mm thick non-absorbing glass slab ($n_g = 1.5$) supporting non-absorbing and ordered cap-shaped water droplets ($n_d = 1.33$) on its back side. By virtue of symmetry, 1/12 of a cap-shaped droplet on a half-equilateral triangle shaped glass surface was simulated. The droplet contact angle θ_c varied between 0° and 90° while the droplet surface area coverage and diameter were constant and equal to $f_A = 55\%$ and $d_p = 2.66$ mm, respectively. The angle of the collimated incident light varied between 0° and 80° . The directional-hemispherical reflectance was found to decrease slightly in the presence of droplets with contact angles $\theta_c \leq 45^\circ$. However, for contact angles larger than the critical angle for

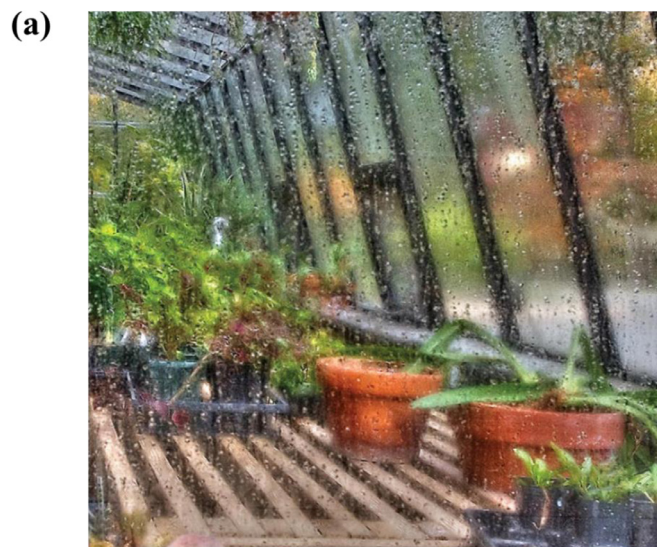


Fig. 1. Water droplets condensed on the inner surface of the glass cover of a (a) greenhouse (Credit: Photograph reproduced with permission from <http://www.MikeSavad.com>) and (b) solar desalination (Photo by Deris Jeannette, ClearDome Solar Thermal and reproduced with permission).

total internal reflection at the droplet/air interface, the normal-hemispherical reflectance increased significantly with increasing droplet contact angle. This was attributed to the fact that total internal reflection at the droplet/air interface reduced the transmittance through the wet glass. The author also stated the need for experimental measurements to validate the numerical simulations and to assess the use of coatings to adjust the droplet contact angle to minimize reflectance.

More recently, Zhu et al. [20] presented a MCRT method to predict the directional-hemispherical transmittance through a non-absorbing glass pane ($n_w = 1.5$) supporting between 350 and 800 non-absorbing cap-shaped water droplets ($n_d = 1.33$) on its back side. Monodisperse or polydisperse droplets either randomly distributed or ordered in a hexagonal pattern on the glass pane surface were investigated. The droplet contact angle θ_c varied between 0° and 180° and the projected surface area f_A between 0 and 90%. The thickness of the glass pane was 3 mm

and the angle of the collimated incident light varied between 0° and 90° . The directional-hemispherical transmittance was found to be independent of droplet diameter and spatial distribution, albeit for non-absorbing droplets [21]. However, it depended on (i) the incident angle θ_i , (ii) the droplet contact angle θ_c , and (iii) the surface area coverage f_A . In fact, the directional transmittance decreased monotonously with increasing incident angle. To describe the effect of droplet contact angle θ_c on the normal-hemispherical transmittance, the authors defined four optical regimes with respect to the critical angle θ_{cr} for total internal reflection at the droplet/air interface. In both Regime I ($\theta_c < \theta_{cr}$) and Regime IV ($\theta_c \geq 180^\circ - \theta_{cr}$), the normal-hemispherical transmittance was found to be nearly independent of contact angle as the droplets scatter the photons forward. In Regime II ($\theta_{cr} \leq \theta_c < 90^\circ$), the normal-hemispherical transmittance decreased rapidly and reached a minimum at 90° . This was attributed to the total internal reflection occurring at the droplet/air interface. A further increase in contact angle between 90° and $180^\circ - \theta_{cr}$ resulted in a rapid increase in the normal-hemispherical transmittance, corresponding to Regime III. In addition, the normal-hemispherical transmittance decreased with increasing surface area coverage in all regimes except Regime I when it slightly increased.

Zhu et al. [21] also predicted the normal-hemispherical transmittance and reflectance of semi-transparent glass pane ($n_w = 1.5$) supporting a large number of absorbing cap-shaped water droplets ($n_d = 1.33$) condensed on their back side. The thickness of the pane was 3 mm and its absorption index k_w varied between 0 and 5×10^{-5} . Monodisperse or polydisperse droplets were distributed either in an ordered hexagonal pattern or randomly on the back side of the pane and featured (i) absorption index k_d ranging between 0 and 5×10^{-2} , (ii) contact angle θ_c between 0° and 180° , (iii) droplet projected diameter d_p between 50 μm and 250 μm , and (iv) surface area coverage f_A from 30% to 55%. The normal-hemispherical transmittance of glass panes supporting non-absorbing droplets was found to be independent of the droplet spatial distribution. For slightly absorbing droplets ($k_d \leq 5 \times 10^{-2}$), the normal-hemispherical transmittance decreased with increasing droplet diameter and volume by virtue of the fact that absorption is a volumetric phenomenon. In addition, the same four optical regimes defined in Ref. [20] for non-absorbing droplets were also observed for slightly absorbing droplets. However, for strongly absorbing droplets, the normal-hemispherical transmittance decreased sharply with increasing contact angle for $\theta_c < 90^\circ$, while remaining constant and independent of the droplet diameter, contact angle, and absorption index for contact angles $\theta_c \geq 90^\circ$. Finally, while the numerical simulations rely on few and realistic assumptions, they have not been validated experimentally.

2.2. Experiments

The effect of water droplets on the transmittance of semi-transparent covers has often been investigated experimentally, under outdoor conditions [4–9,11–13,18]. Cemek et al. [9] measured the total hemispherical transmittance of solar radiation through reduced-scale greenhouses. The greenhouses were covered with a cladding made of a 150-micron thick film of (i) polyethylene (PE), (ii) UV-stabilized polyethylene (UV+PE), (iii) IR absorber polyethylene (IR+PE), or (iv) double-layer polyethylene films (D-Poly). The greenhouses were aligned along the East-West direction in Samsun (42°N), Turkey. The roof of the greenhouses was inclined at an angle of 26° with respect to the horizontal and the sidewalls were vertical. Photographs of the greenhouse roof indicated that the droplet surface area coverage of the roof made of PE, UV+PE, and IR+PE films was 46%, 38%, and 29% with droplet mean diameter of 2.6 mm, 2.0 mm, and 2.6 mm, respectively. Similarly, the droplet surface area coverage on the sidewalls made of PE, UV+PE,

and IR+PE films was 48%, 23%, and 16% with droplet mean diameter of 1.2 mm, 1.2 mm, and 2.6 mm, respectively. Droplets on the D-Poly covers were not characterized owing to the small amount of condensation. The total hemispherical transmittance of solar radiation in the visible was estimated by simultaneously measuring the photon flux density outside and inside the greenhouse using a SunScan analyzer connected to a data logger. The largest decrease in the total hemispherical transmittance, with respect to their dry state, was observed in August and reached about 13%, 11%, and 11% for PE, UV+PE, and IR+PE films, respectively. The authors attributed the decrease in transmittance to the high droplet surface area coverage and volume. Note that the droplet contact angles on the different films were not reported. However, the expected small contact angle on UV+PE films [22] might explain why their transmittance losses were similar to those with the IR+PE films even though the droplet surface area coverage was larger.

Stanghellini et al. [17] performed experiments inside a greenhouse with replaceable covers made of (i) single-pane glass, (ii) double-pane glass, (iii) glass with a pyramid-shaped textured surface, (iv) single glass with antireflecting (AR) coating, (v) uncoated polycarbonate, and (vi) polycarbonate with an anti-drop coating favoring filmwise condensation. Quantum sensors were placed above and below the greenhouse rooftop to measure the total hemispherical transmittance of the covers in the photosynthetically active radiation (PAR) region (400–700 nm). The transmittance of the covers was determined by dividing the photon flux measured simultaneously inside and outside the greenhouse. The results indicated that the effect of droplets on the light transmittance depended on the cover material. Condensation did not affect the transmittance of the glass with a pyramid-shaped texture. This was attributed to the decrease in contact angle with increasing roughness favoring filmwise condensation instead of dropwise condensation. The total hemispherical transmittance of single-pane glass, double-pane glass, single glass with anti-reflective (AR) coating or uncoated polycarbonate decreased by 7%, 9%, 10%, or 18%, respectively, with respect to their dry state. The transmittance of the polycarbonate cover decreased more than that of the glass cover due to the larger droplet contact angle around 84° [23]. Unfortunately, the size distribution, surface area coverage, and contact angle of the water droplets were not reported. Finally, the total hemispherical transmittance of the anti-drop coated polycarbonate slab with small contact angle and thickness of 16 mm increased by 3% due to the presence of a water film.

Bhardwaj et al. [13] performed outdoor tests of solar stills featuring a 2 mm thick cover made of (i) glass, (ii) polyethylene terephthalate (PET), (iii) polycarbonate (PC), or (iv) polymethyl methacrylate (PMMA or acrylic). The covers were facing South and were inclined at an angle of 30° with respect to the horizontal. The contact angle θ_c of water droplets on the glass, PET, PC, and PMMA covers were reported as 30° , 71° , 72.5° , and 82° , respectively. The water production was found to decrease by 40% as the droplet contact angle increased from 30° to 82° . The authors concluded that the transmission of solar irradiation through the wet covers decreased with increasing droplet contact angle. Note, however, that the droplet surface area coverage was not reported and might have varied as droplets slid or dripped more or less depending on the cover material. Similarly, the transmittance may change with cover material due to their different optical properties. The authors recommended the use of hydrophilic cover materials with a low droplet contact angle to maximize water production.

The experimental observations reported to date confirmed that the transmittance in the visible decreased with dropwise condensation on the back side of windows [4–9,12,13,18]. However, most of the previous experimental studies have not systematically characterized the water droplet contact angle, size, and surface area coverage and/or investigated their effect on the window

transmittance and reflectance. This might be due to experimental challenges such as (i) uncontrollable and continuously changing outdoor weather conditions (humidity, temperature, dew point), (ii) contamination on the cover material, and/or (iii) rolling off and entrainment of droplets. These phenomena rendered difficult the measurements of contact angle and surface coverage and limited their achievable range.

The present study aims to experimentally investigate radiation transfer through semi-transparent glass slabs supporting pendant droplets condensed at their back side. To do so, surface-treated glass slabs supporting acrylic droplets with different contact angles and surface area coverages were prepared and systematically characterized. In particular, their normal-hemispherical transmittance and reflectance were measured in the visible and near-infrared parts of the electromagnetic spectrum. The measurements were compared with predictions by the previously developed Monte Carlo Ray Tracing method [20,21] applied to our specific samples.

3. Materials and methods

3.1. Sample preparation

Five different types of glass samples with different surface treatments were prepared to achieve different droplet contact angles including (1) bare soda-lime glass, (2) soda-lime glass coated with commercial water-repellent spray (Rain-X®, USA), (3) soda-lime glass coated with perfluorinated silane (tridecafluoro-1,1,2,2,-tetrahydrooctyl)trichlorosilane, Gelest, USA) referred to as perfluorinated silane, (4) soda-lime glass coated with a perfluorinated silane-treated monolayer of silica nanoparticles, (5) soda-lime glass coated with Teflon AF-2400 (Chemours, USA). Plane-parallel soda-lime silicate glass slabs, 3 mm in thickness with a surface area of $2.5 \times 2.5 \text{ cm}^2$, were kindly provided by Asahi Glass Corporation, Yokohama, Japan. All samples were cleaned with isopropyl alcohol (IPA) prior to any surface treatment.

First, the soda-lime glass slabs coated with water-repellent spray were prepared by spraying the commercial product Rain-X® (620115, 2-in-1 Exterior Detailer and Water Repellent) on a small dry cloth and applying it on one face of the glass sample.

Second, the glass samples coated with perfluorinated silane were prepared by placing the glass slabs inside a closed container filled with silane vapor. Silane with chlorine substituent reacts with hydroxyl groups ($-\text{OH}$) present on the glass surface according to [24]



Note that only reacting bonds are shown in Eq. (1). This reaction permanently grafts perfluorocarbon chains on the surface of the glass substrate to form a hydrophobic coating.

Third, before coating the glass slabs with a monolayer of perfluorinated silane-treated silica nanoparticles, the slabs were placed on a hot plate at 450°C for 30 minutes to remove any oil, dirt, and organic residues. Silica nanoparticles with $307 \pm 20 \text{ nm}$ diameter were synthesized by the Stöber process [25,26]. In this process, tetraethyl orthosilicate (TEOS, 97.0+%, TCI America™), ethanol (EtOH, 200 proof, Rossville Gold Shield), ammonium hydroxide (NH_4OH , VWR Chemicals BDH), and deionized (DI) water were used without any further purification. First, EtOH (8 mL), NH_4OH (0.31 mL), and DI water (1.4 mL) were mixed vigorously with a magnetic stirrer under atmospheric conditions. After 2 minutes of stirring, TEOS (1.5 mL) was quickly added in a single step. The solution was left to stir for 24 hours to allow for the complete growth of nanoparticles. Then, the ethanol/water-based silica nanoparticle suspension was sonicated to break any nanoparticle aggregate. The suspension was drop-casted onto the glass slabs

[27] to obtain a monolayer of silica nanoparticles. Then, the glass slab was heat-treated at 450°C for 1 hour to bond the nanoparticles onto the glass surface and render the coating mechanically robust. Finally, the surface of the silica nanoparticle coating was rendered hydrophobic by depositing perfluorinated silane using the method previously described. The silica nanoparticles before the silane-treatment were characterized using a scanning electron microscope (SEM) (JEOL, JSM-6700F) and an atomic force microscope (AFM) (Bruker, Dimension FastScan).

Fourth, some glass slabs were spin-coated with Teflon AF-2400 followed by heat-treatment on a hot plate at 250°C for an hour. Finally, the sample was baked in a furnace at 340°C for 3.5 hours to achieve a 50 nm thick Teflon film [28].

Following the preparation of the glass slabs with or without surface-treatment, thousands of transparent droplets made of ultraviolet (UV) curable acrylic polymer (Loctite AA 349) were deposited onto the glass substrate. The tip of the needle of a syringe was used to deposit liquid acrylic droplets from the container onto the glass substrate. This procedure was repeated until the desired droplet surface area coverage was achieved. Lastly, the acrylic droplets were cured with a UV lamp at 365 nm (Blak-Ray B-100A, Thermo Scientific Fisher, USA). The use of polymer droplets instead of water droplets facilitated the handling of the samples and eliminated the challenges caused by water droplet motion and evaporation on the glass surface. In addition, the droplet surface area coverage and size distribution could be carefully characterized for each sample and remained the same throughout the experiments. The refractive index of acrylic falls between that of air and that of soda-lime glass [29,30]. Thus, the optical effects caused by the presence of droplets are expected to be qualitatively similar to that of water droplets despite the difference in their refractive indices.

3.2. Droplet characterization

The contact angle of acrylic droplets on the glass substrate was measured using a Drop Shape Analyzer (DSA100, Kruss Scientific, Germany). For each type of glass substrate, the contact angle measurements were repeated for 9 droplets to obtain the mean contact angle $\bar{\theta}_c$ and the associated 95% confidence interval. In addition, the projected droplet diameter d_p and surface area coverage f_A were measured from microscope images captured with a Leica LMIL microscope (Leica Microsystems, USA) connected to a CCD camera (Spot Insight model 4.2, USA). The image analysis software ImageJ was used to manually measure the droplets' location and projected diameter.

3.3. Optical characterization

The normal-hemispherical transmittance and reflectance of the previously described dry and droplet-covered glass slabs were measured using a double-beam ultraviolet-visible (UV-Vis) spectrophotometer (iS50, Thermo Scientific Fisher, USA) equipped with an integrating sphere (EVO220, Thermo Scientific Fisher, USA). Measurements were performed in the visible and near-infrared range between 400 nm and 1100 nm in 1 nm increment.

3.4. Numerical simulations

Fig. 2 shows a schematic of a semi-transparent glass slab of length L , width W , and thickness H covered with polydisperse droplets with contact angle θ_c and projected diameter d_p . The complex index of refraction of the semi-transparent glass was denoted by $m_{g,\lambda} = n_{g,\lambda} + i k_{g,\lambda}$ while that of the droplets was denoted by $m_{d,\lambda} = n_{d,\lambda} + i k_{d,\lambda}$. In order to predict the normal-hemispherical transmittance and reflectance of droplet-covered glasses, the following main assumptions were made: (1) the droplets were

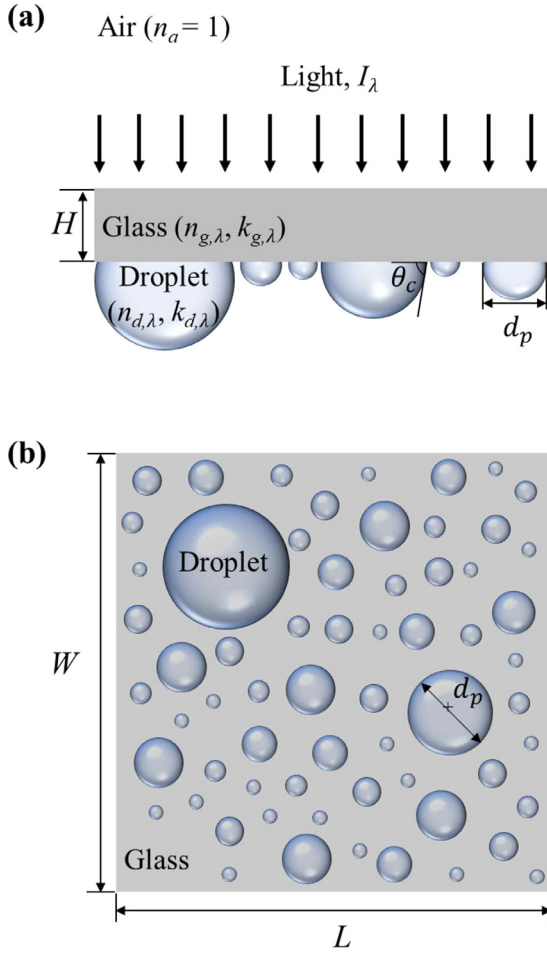


Fig. 2. Schematic of a semi-transparent glass supporting non-absorbing polydisperse droplets (a) front view, (b) top view.

cap-shaped with a constant curvature, (2) all droplets had the same contact angle, (3) all interfaces were optically smooth, and (4) interferences and other wave effects were ignored. Numerical simulations of the normal-hemispherical transmittance and reflectance of non-absorbing droplet-covered glasses were performed using the MCRT method. The algorithm was described in detail in Ref. [20] and need not be repeated. In all simulations, the total number of photon bundles simulated was 10^7 to ensure numerical convergence [20]. Note that simulations of the spectral normal-hemispherical transmittance and reflectance of the Teflon AF-2400 coated soda-lime glass slab with droplet mean contact angle $\bar{\theta}_c = 76.2^\circ$ and surface area coverage $f_A = 45\%$ faithfully simulated the more than 2000 polydisperse droplets with their precisely measured position and projected diameter, as illustrated in Fig. 3. Other simulations assumed droplets to be polydisperse and their diameter followed a normal distribution with an average diameter of $\bar{d}_p = 250 \mu\text{m}$ and standard deviation $\sigma = 150 \mu\text{m}$ to ensure that the droplet diameter was much smaller than the capillary length and that Assumption 1 was satisfied. Note that previous numerical simulations established that the droplet size distribution had no effect on the directional-hemispherical transmittance of glass panes supporting droplets on their back side provided that the droplets were non-absorbing and their diameters were small to ensure that they were cap-shaped [20,21].

The spectral refractive $n_{g,\lambda}$ and absorption $k_{g,\lambda}$ indices of the bare soda-lime silica glass slab used in all simulations were retrieved from the measured normal-normal transmittance $T_{nn,g,\lambda}$

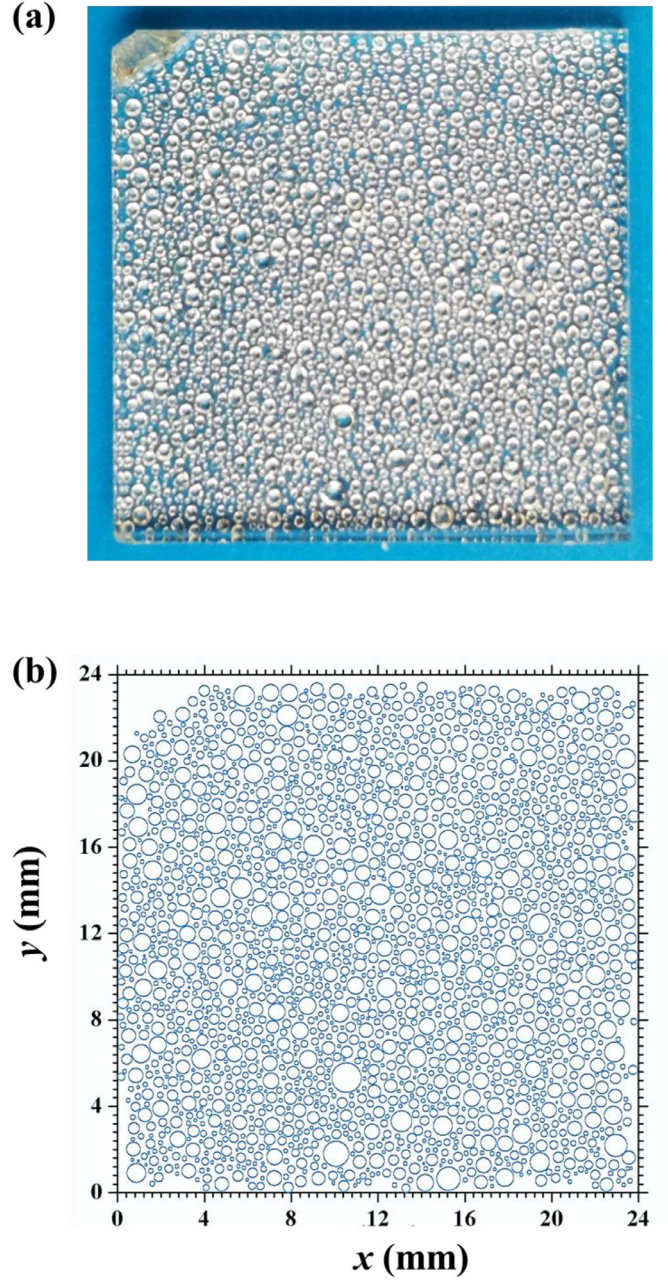


Fig. 3. (a) Photograph of the Teflon-coated glass sample covered with acrylic droplets with contact angle $\bar{\theta}_c = 76.2^\circ$ and surface area coverage $f_A = 45\%$ and (b) corresponding computer-generated droplets.

and reflectance $R_{nn,g,\lambda}$ in the wavelength range from 400 to 1100 nm using the following analytical expressions [31]

$$T_{nn,g,\lambda} = \frac{(1 - \rho_{ag,\lambda})^2 e^{-\kappa_{g,\lambda}H}}{1 - \rho_{ag,\lambda}^2 e^{-2\kappa_{g,\lambda}H}} \quad \text{and}$$

$$R_{nn,g,\lambda} = \rho_{ag,\lambda} \left(1 + \frac{(1 - \rho_{ag,\lambda})^2 e^{-2\kappa_{g,\lambda}H}}{1 - \rho_{ag,\lambda}^2 e^{-2\kappa_{g,\lambda}H}} \right). \quad (2)$$

Here, $\rho_{ag,\lambda}$ is the spectral reflectivity of the air/glass interface and $\kappa_{g,\lambda}$ is the spectral absorption coefficient of the glass slab ex-

Table 1
Summary of the characteristics of the surface-treated glass samples covered with acrylic droplets.

Sample #	Coating	Droplet mean contact angle $\bar{\theta}_c$ (°)	Droplet surface area coverage f_A (%)	Droplet mean diameter \bar{d}_p (μm)
1	None	25.8 ± 2.2	40 ± 5	413 ± 194
2	None	25.8 ± 2.2	49 ± 5	614 ± 360
3	None	25.8 ± 2.2	59 ± 5	507 ± 283
4	Rain-X	37.1 ± 3.8	45 ± 5	368 ± 740
5	perfluorinated silane	54.8 ± 4.6	52 ± 5	606 ± 323
6	perfluorinated silane-treated silica nanoparticles	66.6 ± 4.5	47 ± 5	250 ± 308
7	50 nm Teflon film	76.2 ± 1.6	19 ± 5	428 ± 143
8	50 nm Teflon film	76.2 ± 1.6	34 ± 5	271 ± 161
9	50 nm Teflon film	76.2 ± 1.6	45 ± 5	312 ± 193

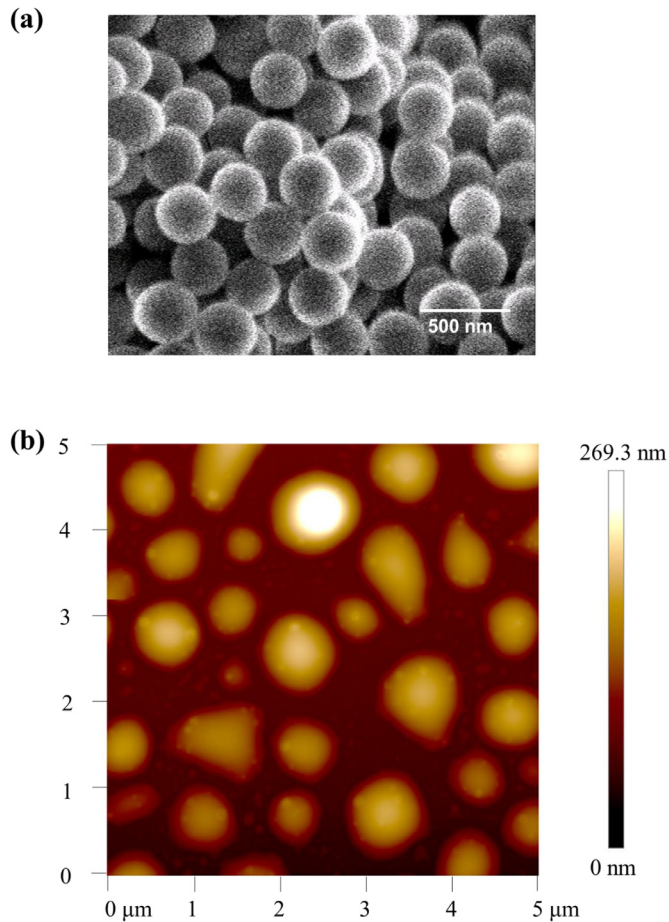


Fig. 4. (a) SEM images of the aggregates of silica nanoparticles synthesized by the Stöber process and (b) AFM image of the silica nanoparticle monolayer deposited onto a glass slab.

pressed as [31]

$$\rho_{ag,\lambda} = \frac{(n_{g,\lambda} - 1)^2 + k_{g,\lambda}^2}{(n_{g,\lambda} + 1)^2 + k_{g,\lambda}^2} \quad \text{and} \quad \kappa_{g,\lambda} = \frac{4\pi k_{g,\lambda}}{\lambda}. \quad (3)$$

Finally, the refractive $n_{d,\lambda}$ and absorption $k_{d,\lambda}$ indices of the acrylic were taken from Refs. [29] and [32], respectively.

4. Results and discussion

4.1. Sample characterization

Fig. 4 shows (a) an SEM image of aggregates of the synthesized silica nanoparticles and (b) an AFM image of the silica nanoparti-

cle monolayer deposited onto a glass slab. The arithmetic average surface roughness of the coating was measured as 35 nm based on AFM images.

Table 1 summarizes the different droplet-covered and surface-treated glass slabs fabricated with different droplet mean contact angle $\bar{\theta}_c$ and surface area coverage f_A . The droplet mean contact angle for the (i) bare glass slabs or glass slabs coated with (ii) water-repellent, (iii) perfluorinated silane, (iv) perfluorinated silane-treated monolayer of silica nanoparticles, and (v) Teflon AF-2400 was $\bar{\theta}_c = 25.8 \pm 2.2^\circ$, $37.1 \pm 3.8^\circ$, $54.8 \pm 4.6^\circ$, $66.6 \pm 4.5^\circ$, and $76.2 \pm 1.6^\circ$, respectively. In addition, the droplet surface area coverage f_A ranged between 19% and 59%. The droplet mean diameter varied between 250 μm and 614 μm. Finally, for the sake of completeness, measurements of the droplet contact angles are reported in Fig. S1 in Supplementary Material. Similarly, Fig. S2 shows representative microscope images of the different samples (Samples 2, 4-6, and 9) and Fig. S3 plots the droplet size distribution for each of the 9 samples presented in Table 1.

4.2. Optical characterization

4.2.1. Optical properties of the soda-lime silicate glass slabs

Fig. S4 in Supplementary Material plots the spectral refractive $n_{g,\lambda}$ and absorption $k_{g,\lambda}$ indices of the soda-lime silicate glass slabs, retrieved from spectral normal-normal transmittance $T_{nn,g,\lambda}$ and reflectance $R_{nn,g,\lambda}$, as functions of wavelength between 400 and 1100 nm. It also plots the refractive $n_{d,\lambda}$ and absorption $k_{d,\lambda}$ indices of acrylic [29,32], as well as that of Teflon AF-2400 [33,34] over the same spectral window. Figure S4 indicates that the retrieved values of $n_{g,\lambda}$ and $k_{g,\lambda}$ differed slightly from those reported in the literature [30,35] but featured similar trends with respect to wavelength. The difference can be attributed to variations in the glass composition.

4.2.2. Spectral normal-hemispherical transmittance and reflectance

Fig. 5 shows the measured spectral normal-hemispherical (a) transmittance $T_{nh,\lambda}$ and (b) reflectance $R_{nh,\lambda}$ as functions of wavelength λ for the dry and droplet-covered glass slabs featuring droplet mean contact angle $\bar{\theta}_c = 25.8^\circ$ and surface area coverage $f_A = 40\%$, 49% , and 59% (Samples 1, 2, 3). Fig. 5 indicates that, for dry glass, the spectral normal-hemispherical transmittance and reflectance decreased with increasing wavelength λ due to absorption attributed to the iron oxide content of the glass [35,36]. In addition, it establishes that the measured spectral normal-hemispherical transmittance $T_{nh,g,\lambda}$ and reflectance $R_{nh,g,\lambda}$ of the dry glass slab were in good agreement with predictions by Eqs. (2) and (3). This observation confirms that the refractive and absorption indices of the glass slabs were properly retrieved. Moreover, Fig. 5(a) shows that the presence of droplets did not affect the spectral normal-hemispherical transmittance $T_{nh,\lambda}$ for droplet contact angle $\bar{\theta}_c = 25.8^\circ$ and surface area coverage f_A between 40% and 60%. These results are consistent with numerical

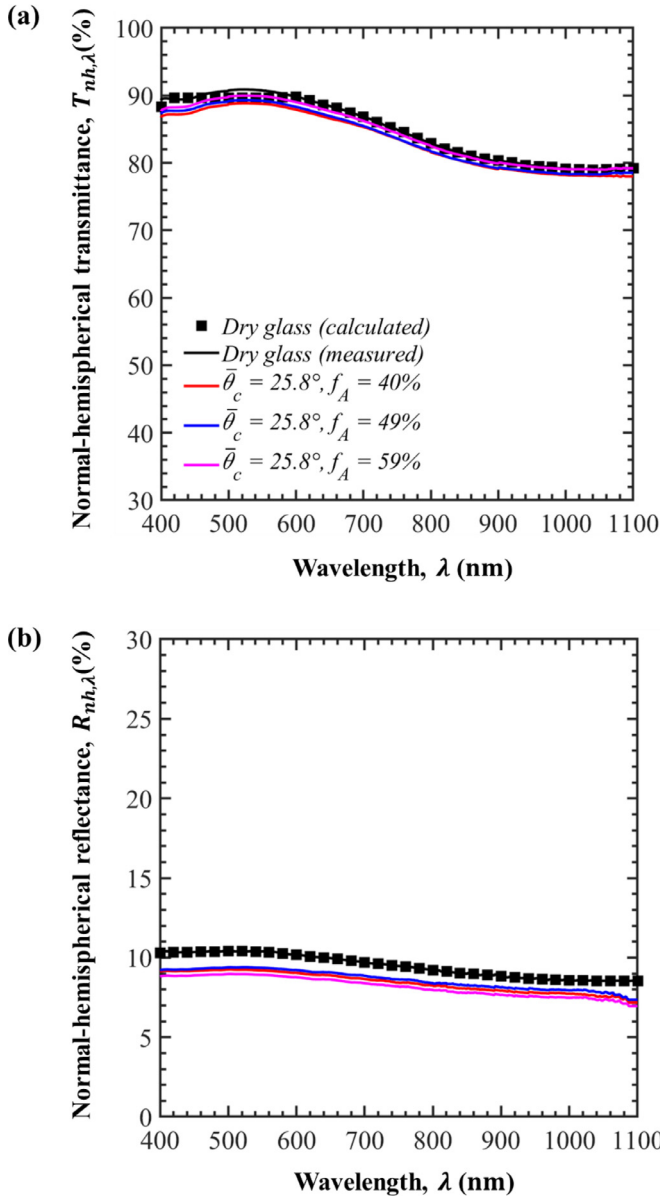


Fig. 5. Normal-hemispherical (a) transmittance $T_{nh,\lambda}$ and (b) reflectance $R_{nh,\lambda}$ as functions of wavelength λ for dry glass and droplet-covered samples with mean contact angle $\bar{\theta}_c = 25.8^\circ$ ($< \theta_{cr}$ in Regime I) and surface area coverage $f_A = 40, 49$, and 59% .

predictions reported by Zhu et al. [20] for non-absorbing water droplets with small contact angle such that $\bar{\theta}_c < \theta_{cr}$ corresponding to Regime I, as previously discussed. Fig. 5(b) shows that the spectral normal-hemispherical reflectance $R_{nh,\lambda}$ decreased slightly due to the presence of droplets, as predicted by Tow [19]. However, the spectral normal-hemispherical reflectance $R_{nh,\lambda}$ was found to be mostly independent of surface area coverage f_A . This can be attributed to the fact that acrylic droplets had a similar refractive index to that of the glass window.

Fig. 6 plots the spectral normal-hemispherical (a) transmittance $T_{nh,\lambda}$ and (b) reflectance $R_{nh,\lambda}$ as functions of wavelength λ between 400 and 1100 nm for dry and droplet-covered glass slabs with droplet mean contact angle $\bar{\theta}_c = 76.2^\circ$ and surface area coverage $f_A = 19, 34$, and 45% (Samples 7, 8, 9). Unlike Fig. 5(a) for $\bar{\theta}_c = 25.8^\circ$, Fig. 6(a) indicates that the spectral normal-hemispherical transmittance $T_{nh,\lambda}$ decreased significantly with increasing droplet surface area coverage f_A across the spectral range considered. This

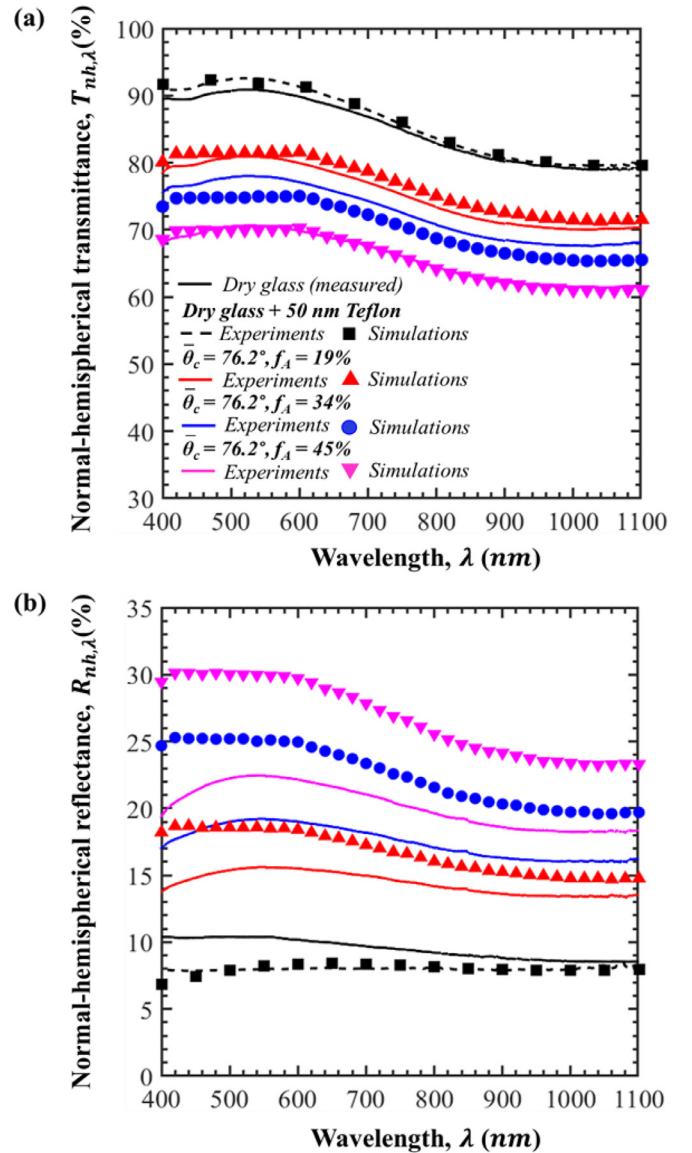


Fig. 6. Normal-hemispherical (a) transmittance $T_{nh,\lambda}$ and (b) reflectance $R_{nh,\lambda}$ as functions of wavelength λ for dry glass, dry glass with 50 nm Teflon coating, and samples with mean contact angle $\bar{\theta}_c = 76.2^\circ$ (Regime II) and surface area coverages $f_A = 19, 34$, and 45% .

situation corresponds to Regime II defined by Zhu et al. [20]. Fig. 6(b) also indicates that the normal-hemispherical reflectance $R_{nh,\lambda}$ increased with increasing droplet surface area coverage f_A due to backscattering caused by total internal reflection at the droplet/air interface [4].

Moreover, Figs. 6(a) and 6(b) compare experimental measurements with predictions obtained from MCRT simulations. Excellent agreement was obtained between experimental measurements and simulations for $T_{nh,\lambda}$ across the spectral window and for all values of surface area coverage f_A considered. However, Fig. 6(b) indicates that the measured normal-hemispherical reflectance $R_{nh,\lambda}$ was systematically smaller than the numerical predictions, particularly with increasing surface area coverage f_A . This discrepancy can be attributed to the presence of the 50 nm thick Teflon coating, which was not accounted for in the MCRT simulations based on geometric optics and ignoring wave effects and interferences occurring in the Teflon thin film. Indeed, Figs. 6(a) and 6(b) also show the spectral normal-hemispherical transmittance $T_{nh,\lambda}$ and reflectance $R_{nh,\lambda}$ of a 3 mm plane-parallel glass slab uncoated and

coated with a 50 nm thick Teflon film as predicted from electromagnetic wave theory using TFCalc software (Software Spectra, Inc., Portland, OR, USA) and the refractive index of Teflon AF-2400 taken from Ref. [33]. These predictions, accounting for interferences, were in excellent agreement with experimental measurements for $T_{nh,\lambda}$ and $R_{nh,\lambda}$ of the dry window coated with 50 nm thick Teflon film. Fig. 6 indicates that the presence of the 50 nm Teflon film slightly increased the normal-hemispherical transmittance but decreased the normal-hemispherical reflectance of the glass pane ($n_g \approx 1.59$) particularly for wavelengths less than 600 nm. Indeed, the presence of the Teflon film ($n \approx 1.28$) reduced the refractive index mismatch at the window/air interface (1.59/1) and thus reduced the amount of total internal reflection occurring at the back surface of the window. In fact, the slight gain in transmittance $T_{nh,\lambda}$ resulted in a similar reduction in reflectance $R_{nh,\lambda}$. For the same reason, the reflectance of any of the dry coated samples was smaller than the uncoated dry glass pane. In fact, their absorptance $A_{nh,\lambda} = 1 - T_{nh,\lambda} - R_{nh,\lambda}$ was nearly identical for all samples with or without coating (see Fig. S5(c)). It increased monotonously with wavelengths above 550 nm to reach 13% at 1100 nm and closely followed the trend observed in the spectral absorption index of soda-lime silica glass [35] (Fig. S4). Similar differences and trends can be observed between the measured and predicted normal-hemispherical reflectance $R_{nh,\lambda}$ of droplet covered glass samples. The absorptance $A_{nh,\lambda}$ of the glass with droplets increased slightly with increasing contact angle and/or surface coverage. This was due to the fact that the acrylic droplets absorbed light in a similar spectral window as the glass, albeit with a smaller absorption index $k_{d,\lambda}$.

4.2.3. Effect of droplet contact angle

Fig. 7 shows the measured spectral normal-hemispherical (a) transmittance $T_{nh,\lambda}$ and (b) reflectance $R_{nh,\lambda}$ as functions of wavelength λ for dry glass and droplet-covered samples with different contact angles $\bar{\theta}_c$ ranging from 25.8° to 76.2° and similar surface area coverage $f_A \approx 48 \pm 4\%$ (Samples 2, 4-6, 9). Fig. 7 indicates that for contact angles $\bar{\theta}_c < \theta_{cr}$, the normal-hemispherical transmittance increased and reflectance decreased slightly with increasing contact angle. However, for contact angles $\bar{\theta}_c \geq \theta_{cr}$, the normal-hemispherical transmittance decreased and the reflectance increased significantly with increasing contact angle.

Moreover, Fig. 8 plots the measured and simulated normal-hemispherical (a) transmittance T_{nh} and (b) reflectance R_{nh} at wavelength $\lambda = 410$ nm as functions of contact angle $\bar{\theta}_c$ for dry and droplet-covered glass slabs with surface area coverage $f_A \approx 48 \pm 4\%$ (Samples 2, 4-6, 9). As a reference, the measured normal-hemispherical transmittance T_{nh} and reflectance R_{nh} at 410 nm of the dry glass slabs with and without coatings were also plotted at their corresponding contact angle with acrylic droplets. This wavelength was selected because the sum of the normal-hemispherical transmittance and reflectance of the samples approached 100% so that absorption by the glass pane and the droplets could be neglected, as assumed by Zhu et al. [20]. Note that the error bars associated with transmittance and reflectance measurements were 4.4% and 1.3%, respectively. They were estimated by considering two main sources of uncertainties during the experiments namely random and instrumentation uncertainties, as presented in Supplementary Material. First, Fig. 8 indicates that, for dry glass slabs, the normal-hemispherical transmittance at $\lambda = 410$ nm increased only slightly by less than 2% due to the presence of coating while the normal-hemispherical reflectance decreased accordingly. For the sake of completeness, Fig. S5 in Supplementary Material plots the spectral normal-hemispherical transmittance $T_{nh,\lambda}$, reflectance $R_{nh,\lambda}$, and absorptance $A_{nh,\lambda}$ of the dry glass slabs with and without coating. Moreover, Fig. 8(a) indicates that the normal-hemispherical transmittance T_{nh} slightly

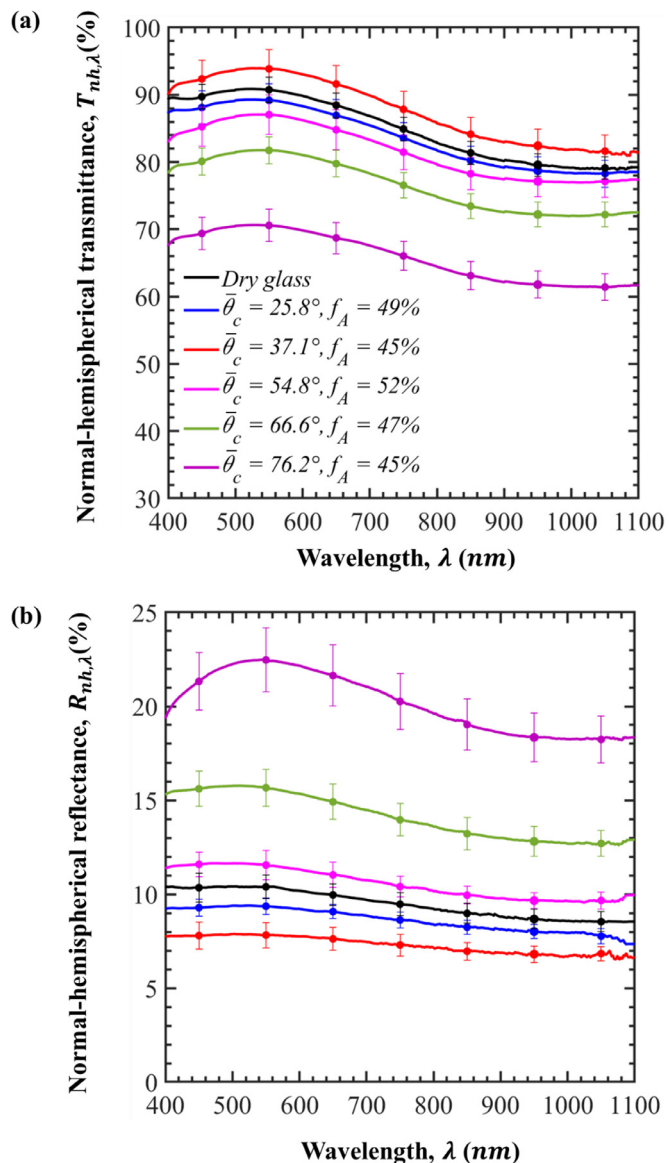


Fig. 7. Normal-hemispherical (a) transmittance $T_{nh,\lambda}$ and (b) reflectance $R_{nh,\lambda}$ as functions of wavelength λ for dry glass and droplet-covered samples with different contact angles ranging from 25.8° to 76.2° (Samples 2, 4-6, 9) and similar surface area coverage around $48 \pm 4\%$.

increased with increasing contact angle $\bar{\theta}_c$ in Regime I until it reached the critical angle for internal reflection at the droplet/air interface predicted by Snell's law as $\theta_{cr} = \sin^{-1}(n_a/n_d) \approx 42.2^\circ$ [31]. In Regime II, corresponding to $\theta_{cr} \leq \bar{\theta}_c < 90^\circ$, the measured normal-hemispherical transmittance decreased rapidly with increasing contact angle $\bar{\theta}_c$. For example, the normal-hemispherical transmittance decreased from 89% to 71% as $\bar{\theta}_c$ increased from 25.8° to 76.2°. The normal-hemispherical transmittance of the glass supporting acrylic droplets is expected to be qualitatively similar to that with water droplets despite the difference in their refractive indices (≈ 1.49 vs. 1.33). Indeed, our previous study [20] established that the normal-hemispherical transmittance of glass cover supporting droplets with surface area coverage $f_A = 90\%$ followed the same trends and was quantitatively similar for droplets with refractive index n_d equal to 1.33 or 1.6, as illustrated in Fig. S6. In addition, the optical Regimes I and II identified numerically by Zhu et al. [20] for water droplets were confirmed experimentally with acrylic droplets (Fig. 8(a)). Moreover, Fig. 8(b) shows that the

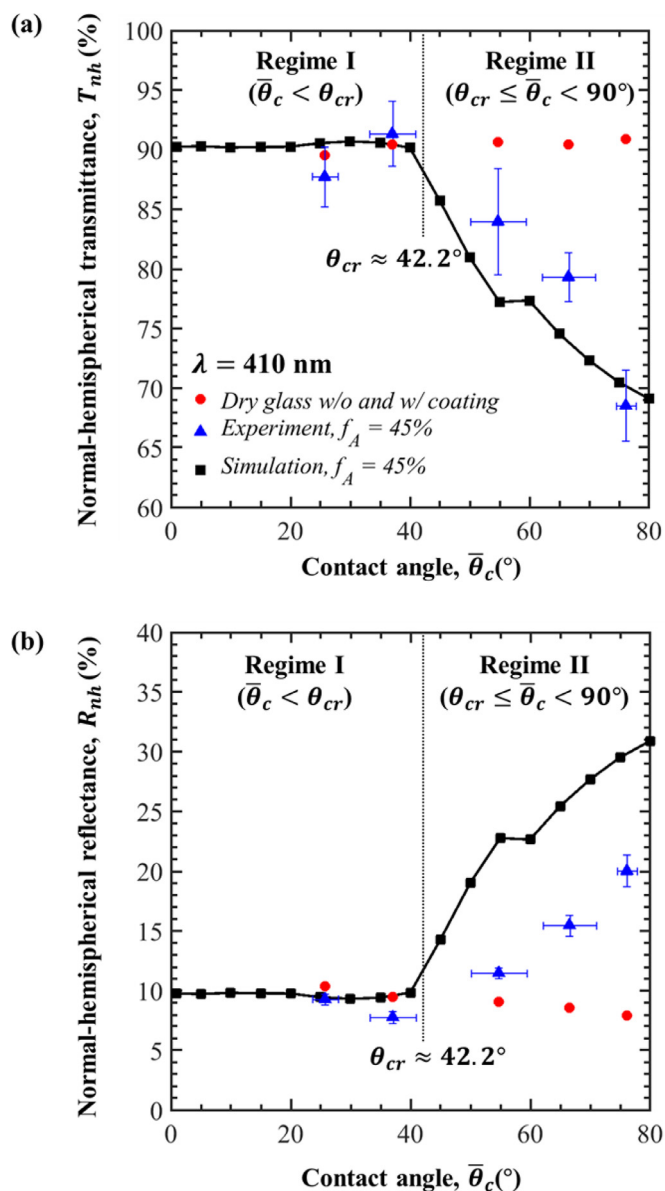


Fig. 8. Comparison of the measured and simulated normal-hemispherical (a) transmittance T_{nh} and (b) reflectance R_{nh} at 410 nm as functions of contact angle $\bar{\theta}_c$ for dry glass slabs with and without coatings and droplet-covered samples with different surface treatments (Samples 2, 4-6, 9) and droplet surface area coverage $f_A \approx 48 \pm 4\%$.

normal-hemispherical reflectance R_{nh} initially decreased ($\bar{\theta}_c < \theta_{cr}$) and then increased ($\theta_{cr} \leq \bar{\theta}_c < 90^\circ$) with increasing contact angle. This could be attributed to the total internal reflection occurring at the droplet/air interface resulting in a decrease in the number of transmitted photons and an increase in the number of back-scattered photons [20].

Figs. 8(a) and 8(b) also indicate that predictions of the normal-hemispherical transmittance and reflectance, obtained assuming $k_w = k_d = 0$, qualitatively followed the same trends as the experimental measurements. However, the measured and simulated reflectance differed quantitatively especially for samples with contact angle $\theta_{cr} < \bar{\theta}_c \leq 90^\circ$ corresponding to Regime II. This discrepancy can be attributed to the fact that, unlike in Regime I (Samples 1-4), droplets in Regime II (Samples 5-9) reflected photons at the droplet/air interface back through the absorbing acrylic droplets and soda-lime glass window, as illustrated in Figs. 8(a) and 8(b) of Ref. [20]. As a result, more photons were not only re-

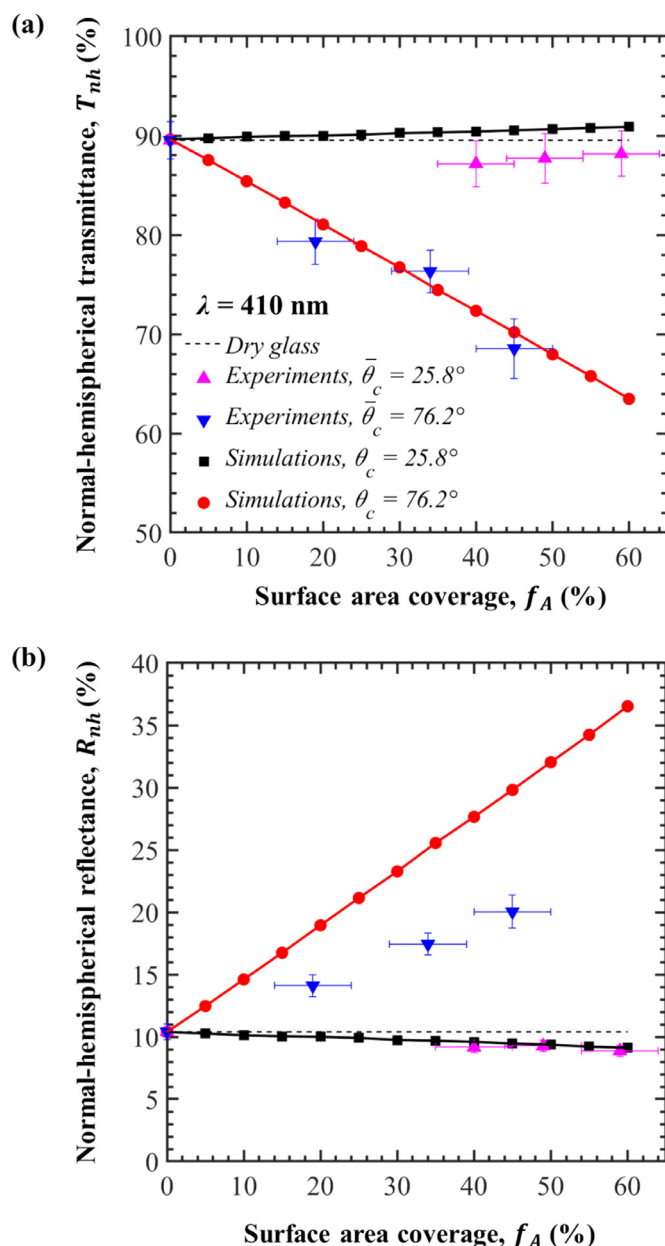


Fig. 9. Comparison of the measured and simulated normal-hemispherical (a) transmittance T_{nh} and (b) reflectance R_{nh} at 410 nm as functions of surface area coverage f_A for dry and droplet-covered samples with mean contact angle $\bar{\theta}_c = 25.8^\circ$ (Samples 1-3) and 76.2° (Samples 7-9).

flected but also absorbed by the droplets and the window in the presence of hydrophobic coating. In fact, Fig. S7 in Supplementary Material plots the normal-hemispherical absorptance $A_{nh,\lambda}$ of the samples with the droplet contact angle (a) $\bar{\theta}_c < \theta_{cr} = 42^\circ$ and (b) $\theta_{cr} < \bar{\theta}_c \leq 90^\circ$ as well as that of the corresponding dry sample. Fig. S7 indicates that the normal-hemispherical absorptance $A_{nh,\lambda}$ of Samples 1-4 ($\bar{\theta}_c < \theta_{cr} = 42^\circ$ - Regime I) was close to that of dry glass. However, the normal-hemispherical absorptance $A_{nh,\lambda}$ of Samples 5-9 ($\theta_{cr} < \bar{\theta}_c \leq 90^\circ$ - Regime II) was larger than that of the dry glass and followed similar trends as the increase in the absorption index spectra of the soda-lime glass and acrylic [Figure S4(b)]. Other discrepancies could be attributed to other effects such as the non-uniformity of the silane coating on the glass slab surface, as visually observed during the droplet deposition, resulting in variations in contact angle, reported in Table 1.

Note also that the predicted normal-hemispherical transmittance and reflectance remained constant for droplet contact angle varying between 55° and 60° . This could be attributed to the fact that photons reflected at the droplet/air interface traveled through the droplet and the glass pane and experienced total internal reflection at the glass/air interface for contact angles $55^\circ < \theta_c < 60^\circ$. They were then transmitted through the glass/droplet and droplet/air interface. The droplet contact angle initiating total internal reflection at the glass/air interface was equal to $\theta_c = 55.5^\circ$, as explained in detail in Supplementary Material.

4.2.4. Effect of droplet surface area coverage

Fig. 9 shows the normal-hemispherical (a) transmittance T_{nh} and (b) reflectance R_{nh} at wavelength $\lambda = 410$ nm as functions of surface area coverage f_A for dry and droplet-covered glass slabs with mean contact angle $\bar{\theta}_c = 25.8^\circ$ and 76.2° (Samples 1-3, 7-9). Fig. 9(a) indicates that, in Regime I ($\bar{\theta}_c < \theta_{cr}$), the normal-hemispherical transmittance T_{nh} increased slightly with increasing surface area coverage f_A . By contrast, in Regime II ($\theta_{cr} \leq \bar{\theta}_c < 90^\circ$), the normal-hemispherical transmittance decreased almost linearly with increasing surface area coverage f_A due to total internal reflection at the droplet/air interface, as explained in Ref. [20]. For example, the normal-hemispherical transmittance decreased from 81% to 71% as the surface area coverage increased from 19% to 45%. Here also, predictions by the MCRT simulations were in excellent agreement with experimental data.

Finally, Fig. 9(b) shows that the normal-hemispherical reflectance R_{nh} at 410 nm decreased slightly with increasing surface area coverage f_A in Regime I ($\bar{\theta}_c < \theta_{cr}$), and increased in Regime II ($\theta_{cr} \leq \bar{\theta}_c < 90^\circ$), as predicted in Ref. [20]. The very good qualitative and quantitative agreements observed between numerical predictions and experimental measurements validate the numerical results reported previously [20,21] as well as the conclusions drawn including the existence of the optical Regimes I and II.

Hydrophobic coatings have been recommended in solar energy applications such as greenhouses due to their anti-fogging [37] and self-cleaning property [38–40]. However, the present results establish that, strictly from a light transfer point of view, hydrophilic cover with droplet contact angle $\bar{\theta}_c < \theta_{cr}$ should be preferred to maximize net solar energy input in applications such as solar collectors, photobioreactors, solar desalination, and greenhouses since dropwise (or filmwise) condensation of hydrophilic surface does not affect solar transmittance significantly [13,16,37].

5. Conclusion

This study investigated experimentally the effects of pendant droplets on the back side of semi-transparent glass slabs on their normal-hemispherical transmittance and reflectance. Soda-lime silica glass slabs without and with surface-treatment and covered with acrylic droplets were prepared with contact angle between 26° and 76° and surface area coverage between 0 and 60%. For droplet contact angle $\bar{\theta}_c$ smaller than the critical angle θ_{cr} for total internal reflection at the droplet/air interfaces (i.e., $\bar{\theta}_c < \theta_{cr}$), the spectral normal-hemispherical transmittance $T_{nh,\lambda}$ was independent of surface area coverage and increased slightly with increasing contact angle. For droplet contact angle such that $\theta_{cr} \leq \bar{\theta}_c < 90^\circ$, the normal-hemispherical transmittance decreased with increasing contact angle and surface area coverage. This was attributed to total internal reflection at the droplet/air interfaces resulting in back-scattering. Predictions of the normal-hemispherical transmittance and reflectance, obtained using the Monte Carlo Ray Tracing method, were in good agreement with experimental measurements thus validating our simulation algorithm and confirming previous conclusions [20]. In particular, this study confirms the

existence of optical Regimes I ($\bar{\theta}_c < \theta_{cr}$) and II ($\theta_{cr} \leq \bar{\theta}_c < 90^\circ$) defined by Zhu et al. [20]. In practice, to minimize the effect of dropwise condensation on the efficiency of solar energy conversion systems, it is recommended to select durable hydrophilic cover materials or apply transparent hydrophilic coatings.

Declaration of Competing Interest

The authors declare that they have no known competing financial interests or personal relationships that could have appeared to influence the work reported in this paper.

CRediT authorship contribution statement

Eylul Simsek: Conceptualization, Investigation, Visualization, Writing - original draft, Writing - review & editing. **Keyong Zhu:** Software, Data curation. **Glareh N. Kashanchi:** Resources. **Megan J. Williams:** Data curation, Writing - original draft. **Tiphaine Galy:** Investigation. **Michal Marszewski:** Resources. **Sarah H. Tolbert:** Resources. **Laurent Pilon:** Supervision, Conceptualization, Resources, Writing - review & editing.

Acknowledgment

This material is based upon work supported, in part, by The Scientific and Technological Research Council of Turkey (TÜBİTAK). The authors would like to thank (i) Prof. Pirouz Kavehpour and Sahar Andalib for their help during the contact angle measurements, (ii) Asahi Glass Corporation for supplying the glass substrates, (iii) Lorna Tokunaga from California NanoSystems Institute at UCLA, and (iv) Deniz Turan for their help with the Teflon coating and AFM images.

Supplementary materials

Supplementary material associated with this article can be found, in the online version, at doi:10.1016/j.jqsrt.2020.107493.

References

- [1] Oshikiri J, Anderson TN. Condensation control in glazed flat plate solar water heaters. In: Proceedings of the 23rd international symposium on transport phenomena, Auckland, New Zealand; 2013. November 19–22.
- [2] National Research Council Sustainable development of algal biofuels in the United States. Washington, DC: National Academies Press; 2012.
- [3] Behera BK, Varma A. Microbial resources for sustainable energy. Cham, Switzerland: Springer International Publishing; 2016.
- [4] Pieters JG, Deltour JM, Debruyckere MJ. Light transmission through condensation on glass and polyethylene. Agric For Meteorol 1997;85:51–62.
- [5] Pollet IV, Pieters JG. Condensation and radiation transmittance of greenhouse cladding materials, part 1: laboratory measuring unit and performance. J Agric Eng Res 1999;74:369–77.
- [6] Pollet IV, Pieters JG. Condensation and radiation transmittance of greenhouse cladding materials, part 2: results for a complete condensation cycle. J Agric Eng Res 2000;75:65–72.
- [7] Pollet IV, Pieters JG. Condensation and radiation transmittance of greenhouse cladding materials, part 3: results for glass plates and plastic films. J Agric Eng Res 2000;77:419–28.
- [8] Geola F, Peiper UM. Outdoor testing of the condensation characteristics of plastic film covering materials using a model greenhouse. J Agric Eng Res 1994;57:167–72.
- [9] Cemek B, Demir Y. Testing of the condensation characteristics and light transmissions of different plastic film covering materials. Polym Test 2005;24:284–9.
- [10] Pieters JG. Interaction effects in simulating the light transmission through condensation drops on greenhouse covers. Trans Am Soc Agric Eng 1997;40(5):1463–5.
- [11] Chaibi MT, Jilar T. Effects of a solar desalination module integrated in a greenhouse roof on light transmission and crop growth. Biosyst Eng 2005;90(3):319–30.
- [12] Zuo L, Zheng Y, Li Z, Sha Y. Experimental investigation on the effect of cover material on the performance of solar still. In: Proceedings of international conference on sustainable power generation and supply (SUPERGEN 2012). Hangzhou, China: IET; 2012. p. 1–4. September 8–9, 2012.

- [13] Bhardwaj R, ten Kortenaar MV, Mudde RF. Influence of condensation surface on solar distillation. *Desalination* 2013;326:37–45.
- [14] Bergman TL, Lavine AS, Incropera FP, Dewitt DP. Fundamentals of heat and mass transfer. 7th edition. New Jersey, NJ: John Wiley & Sons; 2011.
- [15] Hsieh CK, Rajvanshi AK. The effect of dropwise condensation on glass properties. *Sol Energy* 1977;19:389–93.
- [16] Briscoe BJ, Galvin KP. The effect of surface fog on the transmittance of light. *Sol Energy* 1991;46(4):191–7.
- [17] Stanghellini C, Bruins M, Mohammadkhani V, Swinkels GJ, Sonneveld PJ. Effect of condensation on light transmission and energy budget of seven greenhouse cover materials. *Acta Horticult* 2012;952:249–54.
- [18] Geola F, Kashti Y, Peiper UM. Solar radiation transmissivity of greenhouse cladding materials. *Acta Horticult* 2000;534:109–16.
- [19] Tow EW. The antireflective potential of dropwise condensation. *J Opt Soc Am A* 2014;31(3):493–9.
- [20] Zhu K, Huang Y, Pruvost J, Legrand J, Pilon L. Transmittance of transparent windows with non-absorbing cap-shaped droplets condensed on their backside. *J Quant Spectrosc Radiat Transf* 2017;194:98–107.
- [21] Zhu K, Pilon L. Transmittance of semitransparent windows with absorbing cap-shaped droplets condensed on their backside. *J Quant Spectrosc Radiat Transf* 2017;201:53–63.
- [22] Gotoh K, Nakata Y, Tagawa M, Tagawa M. Wettability of ultraviolet excimer-exposed PE, PI and PTFE films determined by the contact angle measurements. *Colloids Surf A* 2003;224:165–73.
- [23] Jankowski P, Ogonczyk D, Kosinski A, Lisowski W, Garstecki P. Hydrophobic modification of polycarbonate for reproducible and stable formation of biocompatible microparticles. *Lab Chip* 2011;11:748–52.
- [24] Ebnesajjad S, Ebnesajjad C. Surface treatment of materials for adhesive bonding. 2nd edition. Elsevier Science; 2014.
- [25] Stöber W, Fink A, Bohn E. Controlled growth of monodisperse silica spheres in the micron size range. *J Colloid Interface Sci* 1968;26(1):62–9.
- [26] Nozawa K, Gailhanou H, Raison L, Panizza P, Ushiki H, Sellier E, Delville JP, Delville MH. Smart control of monodisperse Stöber silica particles: effect of reactant addition rate on growth process. *Langmuir* 2005;21(4):1516–23.
- [27] Mannini M. Molecular magnetic materials on solid surfaces. Firenze, Italy: Firenze University Press; 2008.
- [28] Scheirs J, editor. Modern fluoropolymers high performance polymers for diverse applications. New Jersey, NJ: John Wiley & Sons; 1997.
- [29] Beadie G, Brindza M, Flynn RA, Rosenberg A, Shirk JS. Refractive index measurements of poly (methyl methacrylate) (PMMA) from 0.4 – 1.6 μm . *Appl Opt* 2015;54(31):139–43.
- [30] Rubin M. Optical properties of soda lime silica glasses. *Sol Energy Mater* 1985;12(4):275–88.
- [31] Howell JR, Siegel R, Mengüç MP. Thermal radiation heat transfer. 5th edition. New York, NY: CRC Press; 2010.
- [32] Zhang X, Qiu J, Li X, Zhao J, Liu L. Complex refractive indices measurements of polymers in visible and near-infrared bands. *Appl Opt* 2020;59(8):2337–44.
- [33] Yang MK, French RH, Tokarsky EW. Optical properties of Teflon® AF amorphous fluoropolymers. *J Micro/Nanolith. MEMS MOEMS* 2008;7(3):033010.
- [34] Lowry JH, Mendlowitz JS, Subramanian NS. Optical characteristics of teflon AF fluoroplastic materials. *Opt Eng* 1992;31(9):1982–4.
- [35] Vogt MR, Hahn H, Holst H, Winter M, Schinke C, Kontges M, Brendel R, Altermatt PP. Measurement of the optical constants of soda-lime glasses in dependence of iron content and modeling of iron-related power losses in crystalline Si solar cell modules. *IEEE J Photovolt* 2016;6(1):111–18.
- [36] Synowicki RA, Johs BD, Martin AC. Optical properties of soda-lime float glass from spectroscopic ellipsometry. *Thin Solid Films* 2011;519:2907–13.
- [37] Wu G, Yang Y, Lei Y, Fu D, Li Y, Zhan Y, Zhen J, Teng M. Hydrophilic nano-SiO₂/PVA-based coating with durable antifogging properties. *J Coat Technol Res* 2020;17(5):1145–55.
- [38] Liu Z, Zhang X, Murakami T, Fujishima A. Sol-gel SiO₂/TiO₂ bilayer films with self-cleaning and antireflection properties. *Sol Energy Mater Sol Cells* 2008;92(11):1434–8.
- [39] Zhang L, Dillert R, Bahnemann D, Vormoor M. Photo-induced hydrophilicity and self-cleaning: models and reality. *Energy Environ Sci* 2012;5(6):7491–507.
- [40] Deubener J, Hensch G, Moiseev A, Bornhöft H. Glasses for solar energy conversion systems. *J Eur Ceram Soc* 2009;29(7):1203–10.